Contrib Mineral Petrol
DOI 10.1007/s00410-006-0166-4

ORIGINAL PAPER

Metasomatism of sub-arc mantle peridotites below southernmost South America: reduction of fO_2 by slab-melt

**Jian Wang · Kéiko H. Hattori · Rolf Kilian ·
Charles R. Stern**

Received: 12 January 2006 / Accepted: 17 November 2006

Abstract Quaternary basalts in the Cerro del Fraile area contain two types of mantle xenoliths; coarse-grained (2–5 mm) C-type spinel harzburgites and lherzolites, and fine-grained (0.5–2 mm) intensely metasomatized F-type spinel lherzolites. C-type xenoliths have high Mg in olivine (Fo = 90–91) and a range in Cr# [Cr/ (Cr + Al) = 0.17–0.34] in spinel. Two C-type samples contain websterite veinlets and solidified patches of melt that is now composed of minute quenched grains of plagioclase + Cr-spinel + clinopyroxene + olivine. These patches of quenched melts are formed by decompression melting of pargasitic amphibole. High Ti contents and common occurrence of relic Cr-spinel in the quenched melts indicate that the amphibole is formed from spinel by interaction with the Ti-rich parental magma of the websterite veinlets. The fO_2 values of these two C-type xenoliths range from ΔFMQ –0.2 to –0.4, which is consistent with their metasomatism by an asthenospheric mantle-derived melt. The rest of the C-type samples are free of ''melt,'' but show cryptic metasomatism by slab-derived aqueous fluids, which produced high concentrations of fluid-mobile elements in clinopyroxenes, and higher fO_2 ranging from ΔFMQ +0.1 to +0.3. F-type lherzolites are intensely metasomatized to form spinel with low Cr# (~0.13) and silicate minerals with low MgO, olivine (Fo = ~84), orthpyroxene [Mg# = Mg/(Mg + ΣFe) = ~0.86] and clinopyroxene (Mg# = ~0.88). Patches of ''melt'' are common in all F-type samples and their compositions are similar to pargasitic amphibole with low TiO_2 (<0.56 wt%), Cr_2O_3 (<0.55 wt%) and MgO (<16.3 wt%). Low Mg# values of silicate minerals, including the amphibole, suggest that the metasomatic agent is most likely a slab melt. This is supported by high ratios of Sr/Y and light rare earth elements (REE)/heavy REE in clinopyroxenes. F-type xenoliths show relatively low fO_2 (ΔFMQ –0.9 to –1.1) compared to C-type xenoliths and this is explained by the fusion of organic-rich sediments overlying the slab during the slab melt. Trench-fill sediments in the area are high in organic matter. The fusion of such wet sediments likely produced CH_4-rich fluids and reduced melts that mixed with the slab melt. High U and Th in bulk rocks and clinopyroxene in F-type xenoliths support the proposed interpretation.

Keywords Mantle oxidation state · Mantle wedges · Subduction zone · Adakites

Introduction

Most arc magmas are generated by partial melting of refractory mantle peridotites in the interior of mantle wedges in response to an influx of water, although the

Communicated by J. Hoefs.

J. Wang · K. H. Hattori (✉)
Department of Earth Sciences, University of Ottawa,
Ottawa, ON K1N 6N5, Canada
e-mail: khattori@uOttawa.ca

R. Kilian
Universität Trier, Lehrstuhl für Geologie,
FB VI, Trier 54286, Germany

C. R. Stern
Department of Geological Sciences,
University of Colorado,
Boulder, CO 80309, USA

transfer mechanism of water from subducted slabs to the hot interior of the mantle wedge is still in debate (e.g., Mibe et al. 1999; Hattori and Guillot 2003). Mantle xenoliths from wedges overlying subduction zones are very rare, but studies of these xenoliths suggest that the sub-arc mantle is commonly hydrated and enriched in fluid-soluble alkali and alkali-earth elements (e.g., Brandon and Draper 1996; Arai et al. 2004; Lee 2005). Metasomatism in the sub-arc mantle is commonly accompanied by oxidation, which probably reflects the oxidized nature of aqueous fluids released from subducted slab (e.g., Wood et al. 1990; Ionov and Wood 1992; Brandon and Draper 1996; Parkinson and Arculus 1999; Arai et al. 2003).

Subduction of young oceanic crust may result in partial melting of slabs themselves, producing adakitic arc magmas (e.g., Defant and Drummond 1990). Mantle wedges above such young hot slabs are metasomatized by slab melt (Rapp et al. 1999) and may have significantly different compositions compared to those overlying old slabs that dehydrate but do not melt. Mantle xenoliths from the Cerro del Fraile Quaternary basalts, in the southern Patagonia plateau lava field (Fig. 1), provide samples for the study of the interaction of slab melt with mantle peridotites. Their host basalts were formed in response to upwelling asthenospheric mantle through a slab window that developed due to the subduction of the Chile ridge. The subduction of the young Nazca plate prior to the subduction of the Chile Ridge likely produced slab melt below the study area, similar to the current production of adakitic magmas in the AVZ by the subducted Antarctic plate (Stern and Kilian 1996).

This paper presents the mineralogy, mineral compositions and oxidation conditions of representative samples of mantle xenoliths from Cerro del Fraile, documents different styles of mantle metasomatism and discusses the change in oxidation state during the metasomatism of the underlying mantle.

Geological setting

The late Cenozoic tectonic history of southernmost South America is explained by the subduction of the Nazca and Antarctic plates and Chile Ridge beneath the South American plate. Subduction of the Nazca plate resulted in the formation of a continental arc along the west coast of southernmost South America in Miocene time. This ended when the Chile Ridge collided with the trench at ~14–15 Ma (Cande and Leslie 1986), forming a triple junction between the South American, Nazca, and Antarctic plates near the southern tip of South America. The triple junction has since migrated northwards to its present position, ~46°S (Fig. 1a; Cande and Leslie 1986). The ridge subduction resulted in the formation of a slab window and the extensive eruption of plateau lavas from late Miocene to the recent times (e.g., Ramos and Kay 1992; Gorring et al. 1997; D'Orazio et al. 2000).

In Miocene time, the subducted Nazca plate became progressively younger as the Chile Ridge approached the trench, and likely produced slab melt below the Cerro del Fraile area. Indeed, 13 Ma adakitic magmas produced by the subduction of the young Nazca plate have been documented farther to the north at Cerro Pampa by Kay et al. (1993). This was followed by the arrival of the subducted Chile Ridge, which resulted in the development of a slab window and allowed upwelling of asthenospheric mantle, producing

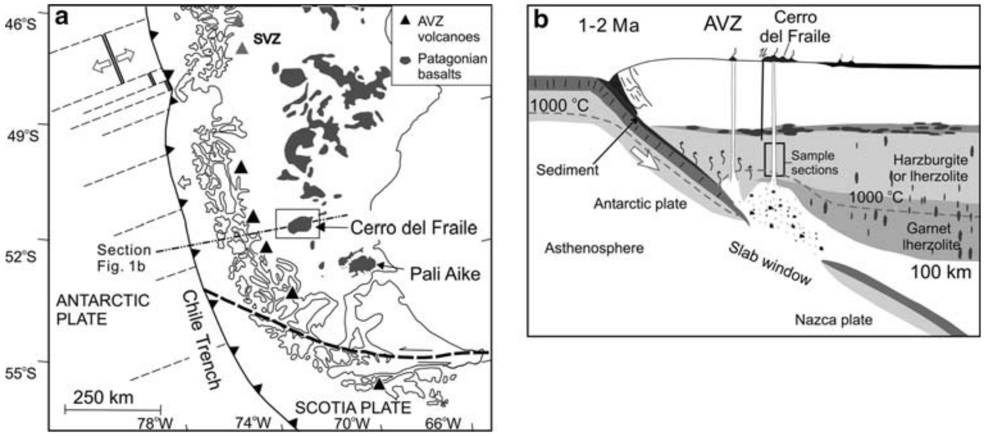

Fig. 1 **a** Map of southernmost South America showing the locations of the Quaternary alkali olivine basalt fields of Cerro del Fraile (CF), Pali-Aike (PA) and other late Cenozoic basalts of Patagonian plateau. Also shown are stratovolcanoes of the Andean Austral Zone (AVZ). **b** Schematic section across Antarctic plate margin-AVZ arc-Cerro del Fraile- Patagonian plateau basalts, including the lithospheric structure below the South American craton (modified after Kilian and Stern 2002)

Patagonian plateau alkali basalt in the area (Fig. 1). The subduction of young Antarctic plate, west of the Ridge, now produces adakitic magmas in the Andean Austral Volcanic Zone (AVZ; Stern and Kilian 1996), located ~25 km west of the Cerro del Fraile area (Fig. 1).

Xenolith petrography and petrology

Mantle xenoliths of 2–30 cm in size occur in basaltic lava flows and diatreme breccias in the area of Cerro del Fraile. We selected nine representative samples similar to xenolith samples described in Kilian and Stern (2002). All are spinel-facies harzburgites and lherzolites, representing peridotites at relatively shallow depths in the underlying lithospheric mantle. Adopting the classification of Arai et al. (2004), two types are recognized based on grain size and textures; coarse-grained (2–5 mm) C-type spinel lherzolite and harzburgite (samples Bxe32-I,-II,-III, Bxe11, Bxe11-I, Bxe31-I, Bxe35-I; Fig. 2a) and fine to medium-grained (0.5–2 mm) F-type spinel lherzolite (samples Bxe1, Bxe22; Fig. 2b). C-type xenoliths show protogranular to porphyroclastic textures with large subhedral grains of olivine and/or orthopyroxene. The F-type shows a weak foliation due to elongated mineral grains. This likely reflects deformation associated with the re-crystallization of these fine-grained peridotites as has been suggested for fine-grained, foliated peridotites by Arai et al. (2004). Therefore, these two types of xenoliths probably represent different areas in the underlying mantle, consistent with different temperatures of equilibration and fO_2 as described below.

C-type spinel lherzolite (sample Bxe35-I) contains olivine (~70 vol%), orthopyroxene (~20 vol%), clinopyroxene (~5 vol%) and spinel (2–3 vol%). The C-type harzburgites (samples Bxe32-I, -II, -III, Bxe11, Bxe11-I, and Bxe31-I), contain veins of websterite (Fig. 2a). The area free of websterite contains olivine (~80 vol%), orthopyroxene (10–15 vol%), clinopyroxene (0–5 vol%) and spinel (<3 vol%). Websterite is coarse grained (2–5 mm) and consists of clinopyroxene (60–70 vol%) and orthopyroxene (30–40 vol%) with minor spinel. Fine blobs and lamellae of spinel are common in pyroxenes in websterite. Patches of solidified "melt" are not common in C-type peridotites, but two samples (samples Bxe11 and Bxe11-I) contain solidified "melt" (~5 vol%), which forms patches (up to 2 mm), and discontinuous veinlets along the grain boundaries (Fig. 2c). These "melt" patches are accompanied by abundant sulfides (10–20 grains/section) and secondary fluid inclusions in minerals adjacent to these patches.

The F-type spinel lherzolites consist of olivine (55–60 vol%), orthopyroxene (~20 vol%), clinopyroxene (5–10 vol%), spinel (~5 vol%) and abundant solidified "melt" (~10 vol%). Solidified "melt" forms veinlets (<0.2 mm) and large patches (up to 2 × 2 mm), which are commonly connected by veinlets (Fig. 2e, f).

Analytical methods

The compositions of minerals were determined using a JEOL 8900 Super Probe at McGill University by wavelength dispersive spectroscopy analysis, and X-ray intensities were simultaneously counted with four analyzers. The operating conditions were 20 kV acceleration voltage, 20 nA beam current and 1 μm beam size. Counting times of 30 s were used for most elements, but 50 s was required for Ca in orthopyroxene and olivine. Due to heterogeneous distributions of minute crystals in "melt patches," the composition of an area 50 × 50 μm was calculated by dividing the area into four areas and determining the composition of each sub-square using a broad beam of 25 × 25 μm. The ZAF correction procedure by JEOL was applied to raw counts.

Attention was paid to the accurate determination of Fe^{3+} contents of spinel because this is critical for the calculation of fO_2. The Fe^{3+} contents are commonly calculated assuming the stoichiometric composition of spinel, but spinel may not be stoichiometric. In our study, four secondary spinel standards with known contents of Fe^{3+} were used to calibrate $Fe^{3+}/\Sigma Fe$ of samples (see Wood and Virgo 1989; Woodland et al. 1992). The inter-grain variation of the calibrated ratios was <10% based on the analysis of 3–5 different grains in each sample (Table 5), and the repeated determination of $Fe^{3+}/\Sigma Fe$ ratios on one grain showed a precision of <5%. The calibrated ratios were slightly lower than those calculated based on stoichiometry (Fig. 3). The fO_2 values were calculated using the olivine-orthopyroxene-spinel oxybarometry of Nell and Wood (1991) and olivine-orthopyroxene-spinel oxybarometry of Ballhaus et al. (1991) (Table 5). Average compositions of the cores of grains were used for the calculation of fO_2 for each sample. The fO_2 values are presented relative to the FMQ buffer because these values are not significantly affected by either temperatures or pressures. For example, a change in 100°C or 1 GPa leads to the difference of only ±0.2 or ±0.3 in logarithmic unit of fO_2, respectively (Wood et al. 1990). We determined Fe^{3+} in the same way as

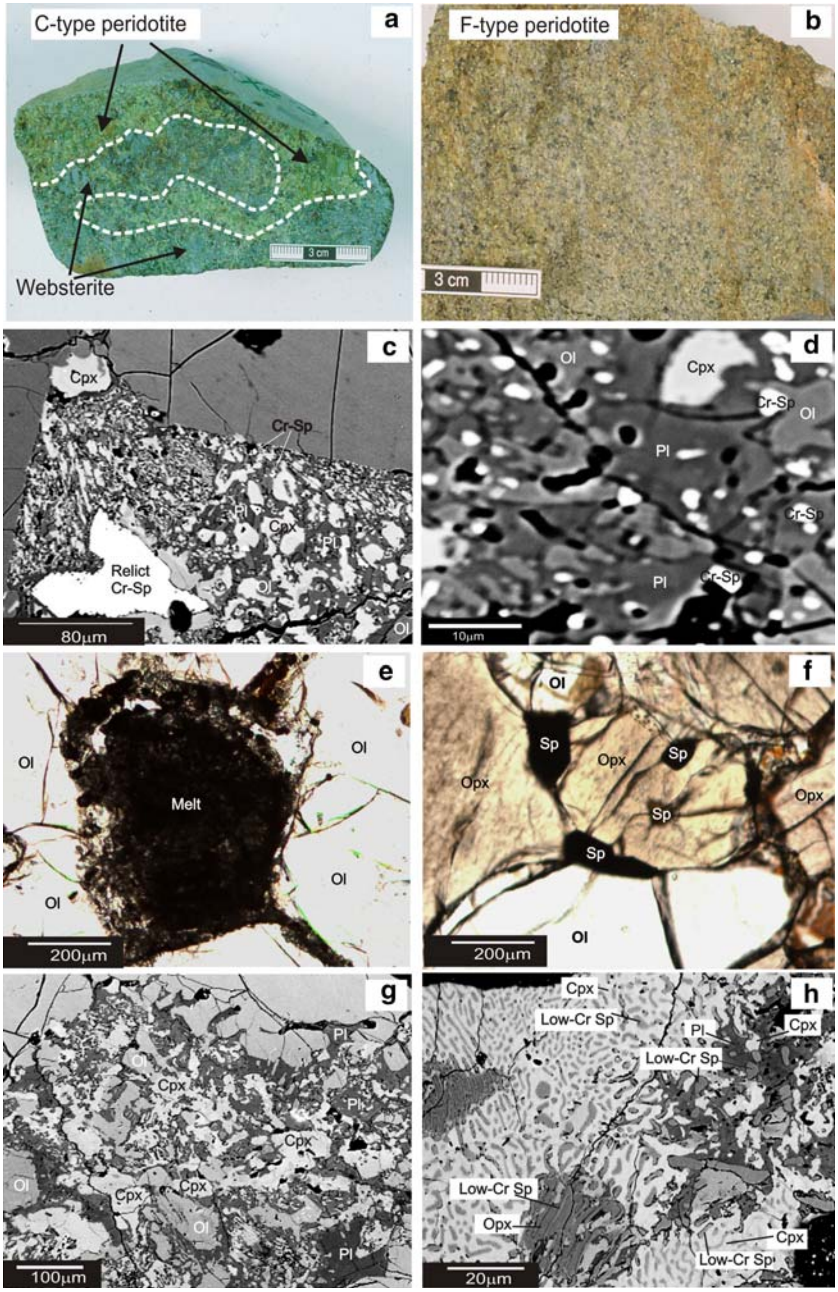

Fig. 2 **a** Photograph of a C-type lherzolite containing websterite vein. The boundary of websterite and perditotites is shown with thick *dotted line*. **b** Photograph of an extensively metasomatized F-type lherzolite xenolith. **c** Back-scattered electron (BSE) image of a veinlet (0.2 mm in width and >0.5 mm in length) in C-type spinel peridotite (sample Bxe11-I). The veinlet is composed of mineral aggregates of plagioclase (Pl) + clinopyroxene (Cpx) + olivine (Ol)+ Cr-spinel (Cr-Sp). **d** BSE image of minute mineral aggregate of solidified ''patch'' melt in C-type peridotite (sample Bxe11-I). **e** Photomicrograph of patch ''melt'' in F-type lherzolite under plain polarized light (sample Bxe1). The patch represents a pseudomorph of pargasitic amphibole with narrow veinlets of solidified ''melt'' radiating from the patch. The patch ''melt'' is dark due to the desseminated grains of fine-grained spinel. **f** Photomicrograph of F-type peridotite under plane polarized light (sample Bxe1). Spinel (Sp) grains occur along grain boundaries of orthopyroxene (Opx) and olivine (Ol) and as inclusions in orthopyroxene. These spinel grains have similar compositions, suggesting that they are equilibrated. **g** BSE image of a solidified ''melt'' in F-type peridotite (sample Bxe22). The ''melt'' is composed of an aggregate of minute clinopyroxene (Cpx) + olivine (Ol) + plagioclase (Pl). Olivine contains dusty spinel inclusions (*bright spots*). **h** Enlarged BSE image of portion of a patch ''melt'' in F-type peridotite (sample Bxe1). Heterogeneous distribution of quenched phases is apparent in this enlarged image, showing different clusters of minerals; a cluster of orthopyroxene (Opx)+ low-Cr spinel (Sp) in the lower left, clusters of clinopyroxene (Cpx)+ low-Cr spinel in the centre top and centre bottom, and a cluster of clinopyroxene + plagioclase (Pl) + low-Cr spinel (Cr_2O_3 <1 wt%) in the upper right

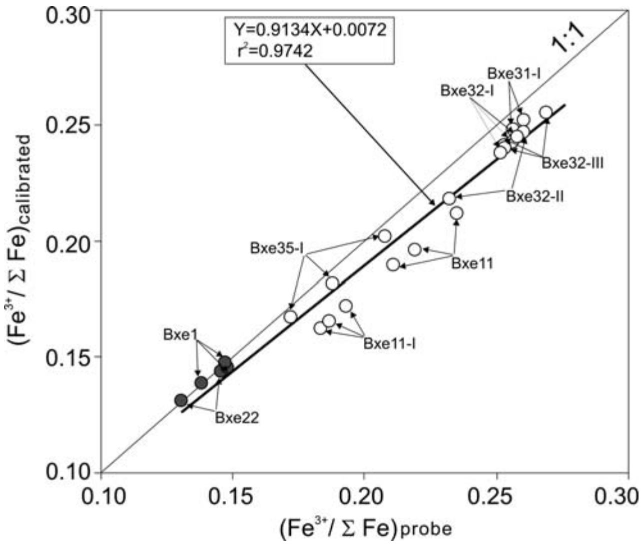

Fig. 3 $Fe^{3+}/\Sigma Fe$ ratios calibrated using spinel standards $(Fe^{3+}/\Sigma Fe)_{calibrated}$, are compared to those calculated assuming stoichiometric composition of spinel $(Fe^{3+}/\Sigma Fe)_{probe}$ from Cerro del Fraile. Each point represents one spinel grain. Quenched spinel crystals in solidified ''melt'' show different compositions even within a single patch and these compositions are not plotted. Calibrated ratios $(Fe^{3+}/\Sigma Fe)_{calibrated}$, were obtained using four spinel standard samples (KLB8304, KLB8311, MBR8305 and KLB8316) with known Fe^{3+} contents and the calculation method described by Wood and Virgo (1989) and Woodland et al. (1992)

Woodland et al. (1992), therefore we believe the uncertainty in the $Fe^{3+}/\Sigma Fe$ calculation is about ±0.025, which also results in an uncertainty in fO_2 of 0.3–0.4 logarithmic units (Woodland et al. 1992). Assuming normal error propagation, the uncertainty in relative fO_2 remains only about ±0.5 logarithmic units.

The major element compositions of bulk rock xenoliths were determined by X-ray fluorescence spectrometry at the University of Heidelberg, Germany, and the trace element contents by inductively coupled plasma mass spectrometry (ICP-MS) at the Memorial University of Newfoundland, Canada. The trace element contents of clinopyroxene were determined by an ICP-MS equipped with a laser ablation system at the Memorial University of Newfoundland, Canada, using the technique described in Taylor et al. (1997).

Mineral chemistry

Olivine

Olivine grains in C-type lherzolites show Fo values ranging from 90 to 91 with moderate CaO (0.04–0.08 wt%) and NiO (0.35–0.39 wt%), whereas olivine in F-type lherzolite shows lower Fo, ~84, and lower CaO (0.03–0.04 wt%) and NiO (0.19–0.20 wt%) than that in C-type lherzolites (Table 1).

Orthopyroxene

Orthopyroxene shows Mg# ranging from 0.91 to 0.92 in C-type and ~0.86 in F-type lherzolites (Table 1). The values are always higher than Fo of co-existing olivine in each sample, which is consistent with equilibrium Fe–Mg exchange between these phases, as observed in other mantle xenoliths (e.g., Qi et al. 1995; Conceição and Green 2004). Orthopyroxene contains moderate CaO (0.57–0.92 wt%) and Al_2O_3 (2.36–3.69 wt%) in both C- and F-type xenoliths. Orthopyroxene grains in F-type lherzolites contain higher TiO_2 (~0.11 wt%) and lower Cr_2O_3 (0.26–0.30 wt%) than those in C-type lherzolites (<0.05 wt% TiO_2, 0.40–0.57 wt% Cr_2O_3). Rims (<50 μm) of orthopyroxene in F-type peridotite have lower Al_2O_3, CaO, Cr_2O_3, and TiO_2, and higher MgO than cores, but the differences are very minor (Table 1). The narrow size of rims suggests that they likely formed during the ascent of the xenoliths to the surface. No zoning was found in orthopyroxene in C-type lherzolites (Table 1).

Clinopyroxene

Clinopyroxene shows different compositions in F- and C-type xenoliths. Clinopyroxene in F-type samples have low-Mg# (~0.88) with relatively high Al_2O_3 (4.06–4.73 wt%), TiO_2 (0.34–0.57 wt%) and Na_2O (0.63–0.85 wt%), and low Cr_2O_3 (0.46–0.66 wt%). Similar to orthopyroxene, rims (<50 μm) contain lower Al, Ti, Cr and Na, and higher Mg than cores (Table 1), but the differences are very minor. Clinopyroxene in C-type xenoliths shows high Mg# (0.91–0.93) with Al_2O_3 (2.97–4.09 wt%), TiO_2 (0.16–0.23 wt%) and Na_2O (0.51–0.89 wt%), and with no apparent compositionally distinct rims.

Spinel

In both C- and F-type xenoliths, spinel occurs as large semihedral grains (<1 mm in C-type; <0.5 mm in F-type), small grains (<0.5 mm in C-type; <0.2 mm in F-type) along grain boundaries of silicate minerals (Fig. 2f), and small (<0.2 mm in C-type; <0.1 mm in F-type) rounded inclusions in olivine and pyroxene (Fig. 2f).

Spinel grains in both C- and F-type xenoliths contain low Fe_2O_3 (up to 3.7 wt%; Table 1; Fig. 5), which is consistent with their origin in mantle peridotites. Spinel in C-type lherzolites shows low Cr# (=Cr/(Cr+Al),

Table 1 Average compositions of minerals in mantle xenoliths from Cerro del Fraile, southern South America

Olivine

Type sample	C-type							F-type	
	Bxe32-I	Bxe32-II	Bxe32-III	Bxe11	Bxe11-I	Bxe31-I	Bxe35-I	Bxe1	Bxe22
SiO_2	40.92	40.75	40.77	41.01	40.91	41.10	41.02	39.66	40.01
FeO	9.42	9.45	9.31	8.88	9.13	9.28	9.12	15.62	15.63
MgO	49.21	49.13	49.11	49.76	49.68	49.53	49.68	44.31	44.41
MnO	0.16	0.14	0.15	0.13	0.13	0.14	0.13	0.23	0.23
CaO	0.07	0.08	0.08	0.04	0.04	0.07	0.06	0.04	0.03
NiO	0.39	0.37	0.37	0.36	0.37	0.37	0.35	0.19	0.20
Total	99.77	99.54	99.42	99.82	99.88	100.1	100.0	99.85	100.3
Fo[a]	90	90	90	91	91	90	91	83	84

Orthopyroxene

Type sample	C-type														F-type			
	Bxe32-I		Bxe32-II		Bxe32-III		Bxe11		Bxe11-I		Bxe31-I		Bxe35-I		Bxe1		Bxe22	
	Core	Rim	Core	Rim	Core	Rim	Core	Rim	Core	Rim	Core	Rim	Core	Rim	Core	Rim	Core	Rim
SiO_2	55.17	55.27	54.80	54.88	55.15	54.90	56.19	55.99	55.69	55.81	54.80	54.82	55.56	55.40	54.02	54.61	54.38	54.69
Al_2O_3	3.55	3.62	3.57	3.58	3.55	3.58	2.36	2.32	2.46	2.41	3.69	3.75	3.52	3.66	3.55	3.00	3.38	3.06
TiO_2	0.06	0.08	0.07	0.07	0.06	0.08	0.08	0.07	0.07	0.07	0.06	0.06	0.04	0.06	0.12	0.06	0.11	0.06
Cr_2O_3	0.52	0.52	0.57	0.55	0.51	0.53	0.46	0.40	0.45	0.41	0.51	0.49	0.39	0.40	0.30	0.22	0.26	0.20
FeO(t)[b]	6.04	6.01	6.26	6.19	6.01	5.97	5.82	5.75	5.92	5.87	6.10	6.11	5.88	5.89	9.91	9.82	9.62	9.79
MgO	32.92	33.08	32.87	32.86	32.93	32.97	34.18	34.03	33.68	33.67	32.82	32.84	33.32	33.30	30.64	30.94	30.70	31.15
MnO	0.15	0.15	0.15	0.15	0.14	0.15	0.14	0.14	0.15	0.14	0.14	0.14	0.14	0.13	0.24	0.23	0.22	0.24
CaO	0.91	0.94	0.92	0.93	0.92	0.95	0.63	0.67	0.65	0.64	0.86	0.87	0.72	0.72	0.57	0.53	0.71	0.56
Na_2O	0.02	0.03	0.04	0.04	0.03	0.05	0.04	0.05	0.03	0.02	0.03	0.03	0.03	0.04	0.03	0.02	0.03	0.01
Total	99.36	99.69	99.25	99.26	99.31	99.17	99.89	99.42	99.10	99.04	99.01	99.13	99.60	99.59	99.38	99.44	99.42	99.77
Mg#[c]	0.91	0.91	0.91	0.91	0.91	0.92	0.92	0.92	0.92	0.91	0.91	0.91	0.91	0.91	0.86	0.86	0.86	0.86

Clinopyroxene

Type sample	C-type														F-type			
	Bxe32-I		Bxe32-II		Bxe32-III		Bxe11		Bxe11-I		Bxe31-I		Bxe35-I		Bxe1		Bxe22	
	Core	Rim	Core	Rim	Core	Rim	Core	Rim	Core	Rim	Core	Rim	Core	Rim	Core	Rim	Core	Rim
SiO_2	52.61	52.72	52.26	52.37	52.24	52.16	53.33	53.24	53.12	52.86	52.12	52.23	52.75	52.72	51.25	51.30	51.47	51.96
Al_2O_3	3.95	4.07	3.94	4.00	3.94	3.97	3.07	3.16	2.97	3.09	4.16	4.23	4.10	4.18	4.67	4.57	4.70	4.34
TiO_2	0.21	0.21	0.17	0.19	0.19	0.19	0.19	0.21	0.19	0.20	0.18	0.18	0.18	0.18	0.57	0.53	0.56	0.42
Cr_2O_3	0.78	0.79	0.79	0.84	0.79	0.83	0.78	0.80	0.68	0.78	0.82	0.77	0.72	0.66	0.64	0.62	0.59	0.53
FeO(t)[b]	2.80	2.89	2.90	2.96	2.79	2.84	2.27	2.34	2.31	2.31	2.84	2.88	2.54	2.53	3.78	3.75	3.81	3.80
MgO	17.34	17.44	17.16	17.29	17.32	17.32	17.17	17.11	17.19	16.98	16.96	16.99	17.07	17.08	15.28	15.45	15.31	15.70
MnO	0.10	0.10	0.09	0.10	0.10	0.10	0.08	0.08	0.07	0.08	0.09	0.08	0.09	0.09	0.12	0.12	0.12	0.12
CaO	21.66	21.50	21.56	21.51	21.59	21.58	22.16	22.08	22.12	22.07	21.49	21.45	21.87	21.91	22.11	22.28	22.23	22.30
Na_2O	0.55	0.63	0.56	0.59	0.53	0.54	0.84	0.85	0.74	0.80	0.63	0.62	0.72	0.71	0.81	0.73	0.78	0.72
Total	100.0	100.3	99.43	99.85	99.49	99.53	99.89	99.85	99.39	99.17	99.29	99.43	100.0	100.1	99.22	99.34	99.55	99.89
Mg#[c]	0.92	0.92	0.91	0.91	0.92	0.92	0.93	0.93	0.93	0.93	0.91	0.91	0.92	0.92	0.88	0.88	0.88	0.88

Spinel

Type sample	C-type														F-type			
	Bxe32-I		Bxe32-II		Bxe32-III		Bxe11		Bxe11-I		Bxe31-I		Bxe35-I		Bxe1		Bxe22	
	Core	Rim	Core	Rim	Core	Rim	Core	Rim	Core	Rim	Core	Rim	Core	Rim	Core	Rim	Core	Rim
Al_2O_3	44.92	45.44	44.54	44.81	45.30	45.39	38.56	38.05	39.43	38.93	48.13	48.34	51.77	51.65	54.07	54.27	54.44	54.16
TiO_2	0.16	0.15	0.14	0.15	0.15	0.15	0.15	0.15	0.16	0.16	0.11	0.12	0.08	0.07	0.08	0.09	0.06	0.08
Cr_2O_3	22.20	21.89	22.52	22.33	21.62	21.63	29.80	29.45	28.55	28.96	18.89	18.80	16.28	16.37	11.80	11.56	11.77	11.71
Fe_2O_3[d]	3.57	2.61	3.36	3.32	3.48	3.29	2.78	3.45	2.44	2.76	3.49	3.35	2.20	2.40	2.59	2.85	2.45	2.65
FeO[d]	9.97	9.57	9.94	10.07	9.68	9.90	9.90	9.94	10.91	10.69	9.36	9.18	8.70	8.56	13.84	13.37	13.79	13.46

Table 1 continued

Spinel

Type sample	C-type														F-type			
	Bxe32-I		Bxe32-II		Bxe32-III		Bxe11		Bxe11-I		Bxe31-I		Bxe35-I		Bxe1		Bxe22	
	Core	Rim	Core	Rim	Core	Rim	Core	Rim	Core	Rim	Core	Rim	Core	Rim	Core	Rim	Core	Rim
MgO	18.99	19.09	18.88	18.86	19.12	19.00	18.46	18.29	17.82	17.95	19.61	19.75	20.33	20.42	17.27	17.62	17.39	17.51
MnO	0.15	0.17	0.17	0.15	0.16	0.15	0.19	0.19	0.18	0.18	0.14	0.14	0.13	0.12	0.17	0.16	0.15	0.15
NiO	0.30	0.28	0.31	0.30	0.31	0.29	0.19	0.20	0.21	0.23	0.29	0.30	0.32	0.28	0.20	0.21	0.20	0.22
Total	100.3	99.20	99.86	99.99	99.82	99.80	100.0	99.76	99.70	99.87	100.0	99.97	99.81	99.90	100.0	100.1	100.2	99.94
Mg/ ($Mg+Fe^{2+}$)	0.77	0.78	0.77	0.77	0.78	0.77	0.77	0.77	0.74	0.75	0.79	0.79	0.81	0.81	0.69	0.70	0.69	0.70
Cr#[e]	0.25	0.24	0.25	0.25	0.24	0.24	0.34	0.34	0.33	0.33	0.21	0.21	0.17	0.18	0.13	0.13	0.13	0.13

Spinel inclusions

Type sample	C-type												F-type			
	Bxe32-I		Bxe32-II		Bxe32-III		Bxe11		Bxe11-I		Bxe31-I		Bxe35-I		Bxe22	
Host	Ol	Opx	Ol	Cpx	Ol	Opx	Ol	Opx	Ol	Cpx	Ol	Opx	Ol	Opx	Ol	Opx
Al_2O_3	46.59	44.89	44.02	45.48	44.99	44.89	35.63	37.02	38.81	39.14	47.66	46.10	52.05	52.37	53.97	52.06
TiO_2	0.16	0.17	0.15	0.15	0.15	0.16	0.17	0.16	0.19	0.17	0.12	0.10	0.05	0.07	0.06	0.09
Cr_2O_3	21.06	21.59	22.82	21.44	21.76	21.82	31.61	29.27	27.95	26.03	18.69	18.36	15.88	15.47	12.12	13.06
Fe_2O_3[d]	1.25	3.76	3.74	3.50	3.83	3.37	3.43	2.98	4.05	5.53	4.02	2.11	2.48	2.47	2.80	3.37
FeO[d]	11.21	9.46	9.69	9.71	9.35	9.61	10.86	10.85	9.71	10.17	8.92	10.40	8.43	8.21	13.22	13.54
MgO	18.05	19.10	18.97	19.12	19.32	19.02	17.36	17.56	18.55	18.10	19.69	19.54	20.55	20.70	17.71	17.22
MnO	0.15	0.15	0.16	0.15	0.14	0.17	0.17	0.17	0.17	0.18	0.15	0.13	0.11	0.11	0.15	0.17
NiO	0.30	0.29	0.29	0.29	0.31	0.29	0.18	0.22	0.20	0.37	0.30	0.30	0.32	0.32	0.22	0.20
Total	98.80	99.56	99.95	99.88	99.89	99.35	99.65	99.39	99.65	99.79	99.66	99.99	99.86	99.71	100.3	99.70
Mg/ ($Mg+Fe^{2+}$)	0.74	0.78	0.78	0.78	0.79	0.78	0.74	0.74	0.77	0.76	0.80	0.77	0.81	0.82	0.70	0.69
Cr#[e]	0.23	0.24	0.26	0.24	0.24	0.25	0.37	0.35	0.33	0.31	0.21	0.21	0.17	0.17	0.13	0.14

Ol olivine, *Opx* orthopyroxene, *Cpx* clinopyroxene

[a] *Fo* forsterite component, 100 × $Mg/(Mg + Fe^{2+})$

[b] Total Fe as FeO

[c] Mg# =$Mg/(Mg+\Sigma Fe)$

[d] Fe_2O_3 contents calibrated using four spinel standards with known $Fe^{3+}/\Sigma Fe$, FeO is the total Fe as FeO minus the calibrated amount of Fe_2O_3

[e] Cr# =Cr/(Cr+Al)

0.17–0.34), TiO_2 (<0.2 wt%) and Fe_2O_3 (2.2–3.7 wt%), and a narrow range in the ratios of $Mg/(Mg + Fe^{2+})$ (0.74–0.81; Fig. 4). They plot in the field of abyssal peridotites on the binary diagram of Cr# and $Mg/(Mg + Fe^{2+})$ (Fig. 4) and ternary diagram of Fe^{3+}–Cr–Al (Fig. 5). Spinel grains in F-type peridotites show low Cr# (~0.13) and $Mg/(Mg + Fe^{2+})$ (~0.69). They have much lower TiO_2 (~0.07 wt%) and mostly lower Fe_2O_3 (2.5–2.8wt%) than those in C-type lherzolite xenoliths. They plot outside or at the margin of the field of abyssal peridotites on the binary and ternary diagrams (Figs. 4 and 5). Spinel inclusions in olivine and pyroxenes are similar in composition to large intergranular grains in the same samples (Table 1), suggesting that the grains are all in equilibrium.

Solidified “melt” patches

Solidified patches of “melt” are common in F-type peridotites. Melt patches also occur in two C-type peridotites that contain abundant websterite veins. These “melt” patches in C-type and F-type peridotites show different textures. Patches in the two C-type xenoliths commonly contain coarse spinel grains with embayments (Fig. 2c). Patches in F-type xenoliths commonly show clusters of different mineral assemblage with symplectic texture (Fig. 2h), such as clusters of clinopyroxene + spinel, orthopyroxene + spinel, and plagioclase + spinel + slinopyroxene.

Melt patches in C- and F-type xenoliths contain different assemblages of quenched minute (<10 μm)

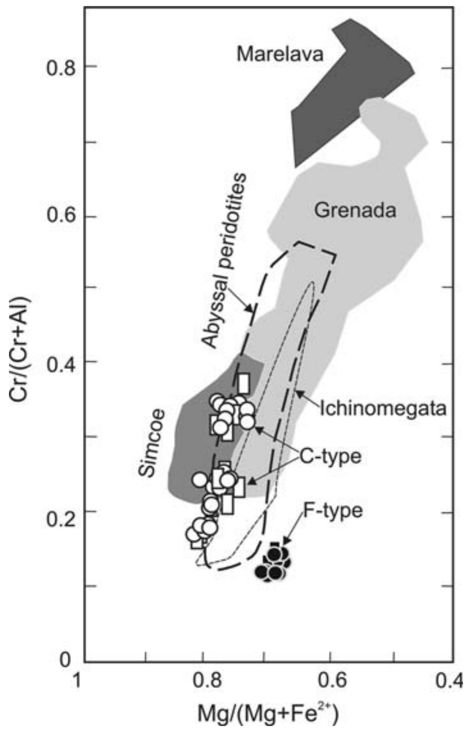

Fig. 4 Plot of Cr# versus Mg/(Mg + Fe^{2+}) for spinel in peridotites from Cerro del Fraile, compared with the data for abyssal peridotites (Dick and Bullen 1984) and sub-arc mantle peridotites. *Open circles* intergranular spinel in C-type, *open rectangles* spinel inclusion in silicate minerals in C-type, *filled circles* intergranular spinel in F-type, *filled rectangles* spinel inclusions in silicate minerals in F-type lherzolite. Data sources of other sub-arc mantle peridotites: Simcoe, western US (Brandon and Draper 1996), Marelava, Vanuatu (Barsdell and Smith 1989), Ichinomegata, Japan (Wood and Virgo 1989; Parkinson and Arculus 1999), Grenada (Parkinson et al. 2003). Note that F-type xenoliths are plotted outside the fields for most mantle xenoliths and abyssal peridotites

minerals. Those in C-type contain plagioclase (30–40 vol%), Cr-spinel (2–5 vol%), clinopyroxene (40–45 vol%) and olivine (10–20 vol%) (Fig. 2c, d), whereas the patches in F-type xenoliths contain these minerals plus orthopyroxene (Fig. 2g,h). Spinel grains in the two types show different compositions. Spinel grains in patches of C-type peridotites contain systematically higher Cr# (~0.57) than those (Cr# = 0.33–0.34) outside the patches, which is consistent with overall high Cr_2O_3 of the composition of patch melt (Table 2). On the other hand, spinel in patches of F-type peridotites contains low Cr_2O_3 (<1 wt%).

Individual mineral phases show compositional variations even within a single patch in both C- and F-type peridotites. The ranges of compositional variation within a single patch are large for clinopyroxene and plagioclase and small for olivine and orthopyroxene. Furthermore, the compositions of pyroxenes and olivine are different from those outside these ''melt'' patches (Table 2). The evidence suggests that the melt in patches was rapidly solidified without equilibration.

The compositions of patches of ''melt'' are different in the C- and F-type xenoliths (Table 2). The patches in C-type have higher Mg# (~0.87), Cr_2O_3 (1.9 wt%) and TiO_2 (1.1 wt%) than those in F-type (Mg# = ~0.83, $Cr_2O_3 \leq$ 0.14, $TiO_2 \leq$ 0.13).

Equilibrium conditions

Thermobarometry

A good positive correlation between Mg# of cores of coexisting mineral phases outside of melt patches suggests equilibrium among these minerals. This is a valid basis for estimating equilibrium P-T conditions and fO_2 of these xenoliths (Table 5). The core compositions of silicate minerals of C-type xenoliths exhibit higher temperatures, when measured with the given geothermometry of 50–150°C than those of F-type xenoliths. The results support the suggestion that these two types

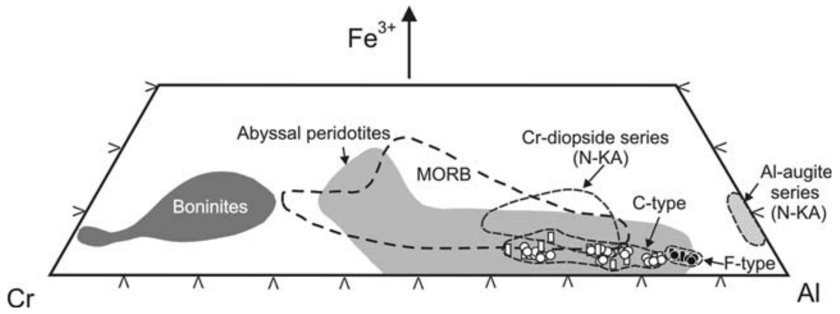

Fig. 5 Ternary diagram of Fe^{3+}–Cr–Al for spinels in the peridotite xenoliths from Cerro del Fraile. Symbols are the same as in Fig. 4. Note that spinel in F-type has lower Cr# than that in C-type peridotites. Data sources: abyssal peridotite, MORB and boninite (Barnes and Roeder 2001); Cr-diopside series (N-KA) and Al-augite series (N-KA) are from north Kamchatka arc (Kepezhinskas et al.1995)

Table 2 Compositions of patch “melt” and quenched phases in the ”melt“ in xenoliths from Cerro del Fraile

Sample phase[a]	Bxe11-I (C-type)					Bxe22 (F-type)						Bxe1(F-type)					
	Cpx	Sp	Ol	Pl	melt	Cpx	Sp	Ol	Pl	melt1	melt2	Cpx	Sp	Pl	Ol	Opx	melt
SiO_2	43.72	0.41	41.11	52.58	45.45	52.54	0.21	39.71	51.24	44.10	41.71	53.34	0.40	51.19	39.77	54.60	39.01
TiO_2	3.77	4.97	<0.04	0.17	1.09	0.72	0.08	<0.04	<0.05	0.13	0.08	<0.04	0.08	<0.05	<0.04	<0.04	0.05
Al_2O_3	10.74	18.60	0.28	28.28	16.54	2.55	64.32	0.04	31.35	18.85	16.79	4.43	65.11	30.88	0.05	4.14	20.45
Cr_2O_3	2.66	37.00	0.08	0.22	1.90	0.23	0.72	<0.04	< 0.02	0.38	0.14	0.01	0.02	< 0.02	<0.04	0.05	0.05
FeO[b]	3.99	22.47	9.38	1.06	4.58	5.29	13.51	14.45	0.30	4.95	5.78	3.95	12.90	0.48	15.27	10.17	6.40
MnO	0.05	0.14	0.14	nd	0.06	0.19	0.12	0.27	nd	0.08	0.17	0.17	0.18	nd	0.29	0.20	0.13
MgO	11.61	12.75	48.34	1.78	17.25	16.31	20.14	44.73	0.06	14.10	16.10	15.37	19.85	0.07	44.38	30.22	16.30
CaO	22.83	0.30	0.27	11.83	10.03	21.30	0.27	0.21	14.07	12.96	16.96	22.50	0.09	14.36	0.18	0.62	15.47
Na_2O	0.82	0.01	0.03	4.21	2.25	0.44	0.01	0.04	3.59	1.16	0.33	0.56	0.03	3.32	0.04	0.04	0.38
K_2O	<0.02	nd	nd	0.21	0.11	<0.02	nd	nd	0.12	0.05	0.02	<0.02	nd	0.13	nd	<0.02	0.02
Total	100.2	96.67	99.70	100.3	99.28	99.58	99.37	99.48	100.7	96.77	98.10	100.3	98.65	100.5	100.1	100.1	98.25
Mg#[c]	0.84	0.50	0.90		0.87	0.85	0.73	0.85		0.84	0.83	0.87	0.73		0.84	0.84	0.82

nd not determined

Cpx clinopyroxene, *Ol* olivine, *Opx*orthopyroxene, *Pl* plagioclase

[a] “Melt” compositions are those of an area, 50 × 50 μm

[b] Total iron as FeO

[c] $Mg^{\#} = Mg/(Mg + \Sigma Fe)$ except for spinel. $Mg/(Mg+Fe^{2+})$ is listed for spinel in which Fe^{2+} is calculated assuming stoichiometric composition

of peridotites originated from different portions of the mantle. When the three thermometers were compared, all yielded similar equilibrium temperatures for C-type xenoliths with differences <20°C except for one sample (Bxe35-I). This one sample yielded unusually high temperature (~1,460°C) using a Ca-in-Opx thermometer (Table 5); the result was discarded because the other two thermometers gave consistent temperatures of 980–1,000°C (Table 5). For F-type lherzolites, the two-pyroxene thermometer of Brey and Köhler (1990) yielded temperatures systematically lower by ~50°C than the two-pyroxene thermometer of Wells (1977), and lower by ~100°C than the Ca-in-Opx thermometer of Brey and Köhler (1990) (Table 5).

We also calculated the temperatures based on the Fe–Mg exchange between olivine and spinel by Ballhaus et al. (1991), but the temperatures were lower by about 100°C than the other results. It is known that olivine-spinel Fe–Mg thermometry may provide unrealistically low temperatures due to low re-equlibration of Fe–Mg exchange at low temperatures (e.g., Sinigoi et al. 1980; De Hoog et al.2004). These unusually low temperatures have been explained by the lower closure temperature for ion exchange between spinel and olivine than that between two pyroxenes.

The absence of garnet and plagioclase in these spinel peridotites limits their crystallization pressures to between 0.8 and 2 GPa (Qi et al. 1995). A pressure of 1.5 GPa was used in calculating the equilibrium temperatures using the two pyroxene thermometers of Brey and Köhler (1990). A difference of 0.5 GPa can result only with 5–10°C and 20–30°C temperature differences for Brey and Köhler's two-pyroxene thermometer and Ca-in-Opx thermometer, respectively.

Oxybarometry

The calculation of fO_2 used the temperature obtained by Wells' two pyroxene thermometer because it has been used for fO_2 calculations of mantle peridotites by many workers and this keeps our calculations consistent with their results. Although different thermometers yielded different temperatures for F-type xenoliths (Table 5), these differences, of ~100°C, only result in a negligible discrepancy in fO_2 of <0.2 logarithmic unit. The pressure for the fO_2 calculations is assumed to be 1.5 GPa.

The values of fO_2 were calculated using the equations of Nell and Wood (1991) and Ballhaus et al. (1991) (Table 5). The two methods gave comparable fO_2 with differences of <0.33 logarithmic unit (Table 5), but the oxybarometry of Ballhaus et al. (1991) yielded systematically lower fO_2 for C-type xenoliths and higher values for F-type xenoliths than the oxybarometry of Nell and Wood (1991). This paper uses the fO_2 value based on the equation of Nell and Wood (1991).

The C-type peridotite yielded fO_2 ranging from ΔFMQ –0.39 to +0.31 (average ΔFMQ –0.03 ± 0.28) and the values are not correlated with Cr# in spinel (Fig. 6; Table 5). Two samples with abundant patch “melt” show slightly reduced fO_2, ΔFMQ –0.37 to –0.18. Intensely metasomatized F-type peridotites yield relatively low fO_2 as low as ΔFMQ –1.1 (Fig. 6; Table 5).

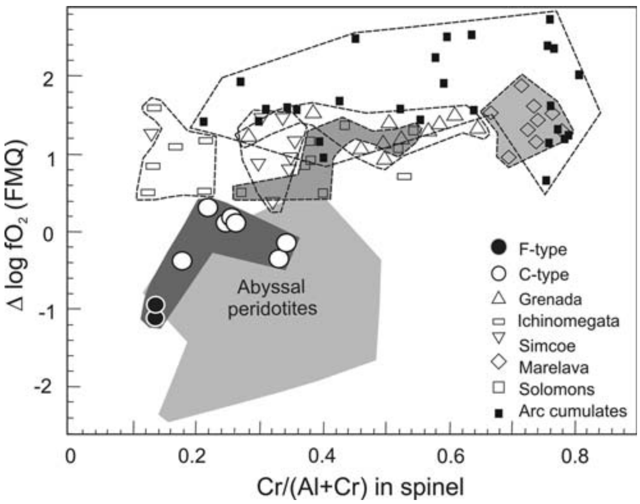

Fig. 6 Values of fO_2 relative to FMQ buffer ΔfO_2 (FMQ) versus Cr# in spinel for peridotites from Cerro del Fraile compared with arc cumulates (Ballhaus, 1993), abyssal peridotites (Bryndzia and Wood 1990) and sub-arc mantle peridotites. Data source for sub-arc mantle peridotites: Simcoe (Brandon and Draper 1996), Ichinomegata, Japan (Wood and Virgo 1989; Parkinson and Arculus 1999), Grenada, Marelava, and Solomons (Parkinson and Arculus 1999; Parkinson et al. 2003)

Discussion

Parental magmas for websterite

Websterite veinlets in C-type peridotites consist of two pyroxenes, minor Al-rich spinel and abundant sulfides (10 grains/section). Abundant fluid inclusions along cracks in olivine and pyroxenes around the websterite veinlets suggest that the parental magmas to these websterite veins were high in volatiles. The bulk composition of websterite is also high in TiO_2 (~1.1 wt%; Table 4) and shows ocean island basalt-like geochemical signature (Fig. 8d) similar to the basalts hosting the xenoliths (Table 4). Therefore, the websterite is interpreted as a cumulate of melt derived from the asthenospheric mantle. The development of the slab window and asthenospheric melts that generated the host basalts in the area took place in the past 2 Ma. It is this young event, <2 Ma, that produced the websterite and the associated Ti-rich metasomatism.

Origin of patch ''melt''

The patches of solidified ''melt'' could be a melting product of pre-existing minerals or invaded melt from the parental magmas for the host volcanic rocks. The latter possibility is rejected because the compositions of the ''melt'' patches in both C- and F-type peridotites show high CaO and MgO and low K_2O, which is significantly different from the compositions of host basalts (Tables 2 and 4). Instead, the compositions of the ''melt'' patches in both types of xenoliths are similar to those of pargasitic amphibole (Table 3), suggesting that these ''melt'' patches are likely a breakdown product of amphibole. Pargasitic amphibole is common in hydrated peridotite xenoliths from sub-arc mantle, such as Nunivak Island, Alaska (Francis 1976), Megata, Japan (Abe et al. 1998), South Kamchatka, Russia (Arai et al. 2003) and Iraya, Philippines (Arai et al. 2004) (Table 3).

Pargasitic amphibole may melt during decompression or heating. Mantle peridotites in the area may have been heated by upwelling asthenospheric mantle during the development of a slab window, but this possibility is discounted because of disequilibrium mineral assemblages and compositions of minerals in individual patches. The melting must have occurred quickly with little re-equilibration time after melting and prior to quenching. Therefore, we conclude that a rapid rise of these xenoliths to the surface most likely led to decompression melting of the pargasitic amphibole in the xenoliths. Solidified ''melt,'' that also has compositions similar to pargasitic amphibole, has been reported in mantle xenoliths from other areas and has also been explained by decompressional melting of amphibole. Examples include melts in xenoliths from Nunivak Island, Alaska (Francis 1976), western Victoria, Australia (Yaxley et al. 1997), southeastern Australia (Yaxley and Kamenetsky 1999) and western Eifel, Germany (Shaw and Klügel 2002; Ban et al. 2005).

Kilian and Stern (2002) described veinlets of adakitic ''melt'' that contain high SiO_2 (>60 wt%) and Na_2O (>6 wt%), and low MgO and CaO in xenoliths from Cerro del Fraile (Table 4). We did not observe such ''melt'' in our samples.

Origin of amphibole

The inferred compositions of pargasitic amphiboles are different in F-type and C-type xenoliths (Table 2). The latter shows higher Cr_2O_3 (1.9 wt%) and TiO_2 (~1.1 wt%) than those in F-type peridotites (Table 2). Furthermore, patches in C-type contain relatively large spinel grains with embayment (Fig. 2c), suggesting that the pargasitic amphibole likely formed after spinel during their reaction with a metasomatizing agent. Spinel grains in C-type all contain low TiO_2, <0.15–0.16 wt%, whereas the melt patches in these xenoliths contain high TiO_2, suggesting that the metasomatizing agent contained high TiO_2.

Table 3 Compositions of amphiboles in other sub-arc mantle peridotites

Area sample	Nunivak Island, Alaska						Megata, Japan		North-Kamchatka			Batan, Philippines	
	10006	10013	10016	10050	10052	10067	I-610A	I-014A	val55/ 4-2	val55/ 4-4	Val55/12	A	B
SiO_2	45.99	44.54	46.75	43.57	44.04	43.85	43.80	44.44	43.11	42.86	42.96	42.20	48.96
TiO_2	0.08	0.38	0.11	0.95	0.43	0.37	0.85	0.79	2.11	2.10	2.91	1.85	0.30
Al_2O_3	12.91	13.42	11.51	14.18	14.64	14.54	14.67	12.63	12.18	12.83	11.44	12.87	12.90
Cr_2O_3	3.14	2.85	2.55	1.91	1.50	1.97	0.15	1.09	0.01	0.02	0.00	1.27	0.05
FeO(t)[a]	3.42	4.13	3.29	3.90	3.14	4.50	6.89	6.79	10.97	10.13	11.62	6.49	9.24
MnO	0.07	0.11	0.11	0.06	0.08	0.11	0.21	0.12	0.13	0.11	0.11	0.17	0.06
MgO	18.45	17.68	19.01	17.79	18.16	17.80	16.48	16.55	14.77	15.29	14.81	16.60	13.56
CaO	9.07	9.79	9.43	10.89	11.14	9.32	11.50	11.49	10.40	10.77	11.38	11.97	10.01
Na_2O	4.79	3.83	4.39	2.96	3.18	3.84	2.17	2.25	3.08	3.49	2.47	1.85	1.56
K_2O	0.92	1.31	0.72	1.63	1.09	1.24	0.65	0.78	0.51	0.45	0.66	1.10	1.18
Total	98.84	98.04	97.87	97.83	97.39	97.54	97.37	96.93	97.27	98.05	98.36	96.49	98.02
Mg#[b]	0.91	0.88	0.91	0.89	0.91	0.88	0.81	0.81	0.71	0.73	0.69	0.82	0.72
Reference	Francis (1976)						Abe et al. (1998)		Kepezhinskas et al. (1995)			Schiano et al. (1995)	

[a] Total Fe as FeO

[b] Mg# = Mg/(Mg+ΣFe)

The metasomatizing agent may have been either an aqueous fluid or a melt. In the study area, aqueous fluids could be those released from the subducted slab. Melts may be arc magmas or melts from asthenospheric mantle formed during the development of the slab window that generated the host Cerro del Fraile basalts. Aqueous fluids released from slabs and arc magmas are both low in Ti. Therefore, we discount these possibilities. For example, amphiboles in mantle xenoliths from Nunivak Island are considered to have formed during the reaction of spinel with volatiles released from arc magmas (Francis 1976). These amphiboles show lower Ti contents than those in our C-type xenolith samples (Tables 2 and 3).

Table 4 Composition of host basalts, and veins of websterite and adakitic melt in xenoliths from Cerro del Fraile

Sample	Basalt 1	Basalt 2	Websterite	Adakitic vein[c]
SiO_2	48.35	48.78	40.3	60.30
TiO_2	1.51	1.57	1.06	0.21
Al_2O_3	16.9	16.67	7.9	20.30
Cr_2O_3	0.02	0.02	0.07	0.35
FeO(t)[a]	10.51	10.13	17.57	1.10
MnO	0.17	0.17	0.21	0.05
MgO	6.99	6.93	26.53	3.30
CaO	7.78	7.67	5.87	6.60
Na_2O	4.16	4.14	1.01	6.20
K_2O	1.02	1.14	0.22	0.65
P_2O_5	0.93	0.89	0.14	nd
Total	98.31	98.07	100.9	99.06
Mg#[b]	0.54	0.55	0.74	0.84

nd not determined

[a] Total Fe as FeO

[b] Mg#=Mg/(Mg+ΣFe)

[c] Average composition (n = 800) of adakitic veinlets (Kilian and Stern 2002)

The contents of Ti are high in the websterite veins in amphibole-bearing C-type xenoliths (Table 4). Therefore, we suggest that the amphibole in C-type xenoliths formed by reactions with the asthenosphere-derived parental magma for these websterite veins during the development of a slab window. During the metasomatism, Al in the pre-existing spinel was incorporated into the newly formed amphibole, which resulted in high Cr# of the relict spinel grains.

Pargasitic amphiboles in F-type peridotites contained slightly higher CaO and lower Mg# and Ti compared to amphiboles in C-type (Table 2). Furthermore, there is no embayed spinel grain in patches of "melt" and no clinopyroxene grain around the patches. The evidence may suggest that pargasitic amphiboles may have formed at the expense of clinopyroxene. Low Mg# of the amphibole suggests that they likely formed together with other low Mg silicates. Furthermore, the amphibole compositions are similar to those in the xenoliths that were metasomatized by slab-melt, such as those in Batan Island, Philippines (Schiano et al. 1995; Table 3) and Al-augite series xenoliths in north Kamchatka, Russia (Kepezhinskas et al. 1995; Table 3). Moreover, minute spinel grains in the "melt" patches are compositionally similar to the Al–Fe–Mg spinel in Al-augite series xenoliths from north Kamchatka arc. Remarkable similarities of amphiboles between Cerro del Fraile F-type samples and mantle xenoliths affected by slab melt suggest that the pargasitic amphiboles in these samples likely formed by similar processes associated with metasomatism by slab-melt.

Table 5 Oxygen fugacity values and parameters of olivine, orthopyroxene and spinel in the mantle xenoliths from Cerro del Fraile

Type samples	C-type							F-type	
	Bxe32-I	Bxe32-II	Bxe32-III	Bxe11	Bxe11-I	Bxe31-I	Bxe35-I	Bxe1	Bxe22
Olivine									
X_{Fe}	0.097	0.097	0.096	0.091	0.093	0.095	0.093	0.165	0.165
X_{Mg}	0.903	0.903	0.904	0.909	0.907	0.905	0.907	0.835	0.835
Orthopyroxene									
Enstatite	0.889	0.885	0.889	0.900	0.897	0.889	0.895	0.834	0.836
Ferrosilite	0.094	0.097	0.093	0.088	0.091	0.095	0.091	0.155	0.150
M1(Fe) [a]	0.086	0.090	0.085	0.083	0.085	0.087	0.083	0.144	0.139
M2(Fe) [a]	0.089	0.092	0.089	0.085	0.087	0.091	0.087	0.149	0.144
Spinel									
Cr#	0.25	0.25	0.24	0.34	0.33	0.21	0.17	0.13	0.13
$(Fe^{3+}/\Sigma Fe)^{b}_{probe}$	0.26	0.25	0.26	0.22	0.19	0.26	0.19	0.14	0.14
$(Fe^{3+}/\Sigma Fe)^{c}_{calibrated}$	0.24	0.23	0.24	0.20	0.17	0.25	0.19	0.14	0.14
SD(%)[d] for $(Fe^{3+}/\Sigma Fe)_{calibrated}$	1.17	8.28	3.47	5.78	3.01	1.37	10.33	3.37	6.70
$Mg/(Mg+Fe^{2+})$	0.77	0.77	0.78	0.77	0.74	0.79	0.81	0.69	0.69
$\log a_{Fe3O4}$	–2.07	–2.11	–2.09	–2.27	–2.34	–2.04	–2.36	–1.90	–1.95
Temperature and oxygen fugacity									
T°C (Wells)[e]	1036	1031	1041	955	963	1023	1000	901	901
T°C (BK)[f]	1029	1028	1028	925	932	1018	982	855	857
T °C (BK)[g]	1030	1035	1035	942	951	1018	1458	929	977
$\log(fO_2)FMQ$[h]	–0.03	–0.15	–0.06	–0.45	–0.55	–0.01	–0.72	–0.80	–0.90
$\log(fO_2)FMQ$[i]	0.14	0.12	0.14	–0.18	–0.37	0.31	–0.39	–0.92	–1.08

[a] M1 (Fe), M2 (Fe) = Fractions of Fe at M1 and M2 sites, calculated following the method in Wood et al. (1990)

[b] Calculated assuming stoichiometric composition of spinel

[c] Calibrated using the four spinel grains with known Fe^{3+} contents

[d] Standard deviation calculated based on cores of 3–5 grains in each sample

[e] Calculated based on two-pyroxene thermometer (Wells 1977)

[f] Calculated based on two-pyroxene thermometer (Brey and Köhler 1990)

[g] Calculated based on the Ca-in-OPX thermometer (Brey and Köhler 1990)

[h] Calculated following the method of Ballhaus et al. (1991) using the Fe^{3+} contents of spinel assuming its stoichiometric composition

[i] Calculated following the method of Nell and Wood (1991) using the calibrated contents of Fe^{3+}

Origin of the two types of peridotites

C-type peridotites

The mineralogy and mineral compositions of the C-type xenoliths are similar to mantle peridotites from many parts of the world. This is supported by the plots of samples in the olivine-spinel mantle array of Arai (1994) (Fig. 7). The compositions of spinel overlap with the field of abyssal peridotites (Figs. 4, 5 and 7). The evidence supports the proposal that the subcontinental lithospheric mantle below southernmost South America increased its size by stacking of oceanic lithosphere (Stern et al. 1999; Carlson et al. 2005).

The modal metasomatism, the formation of websterite veins and high Ti pargasitic amphibole, in C-type peridotites was produced by interaction with Ti-rich asthenospheric melt, as described in the previous section. Cryptic metasomatism has also affected C-type peridotites. This metasomatism did not produce

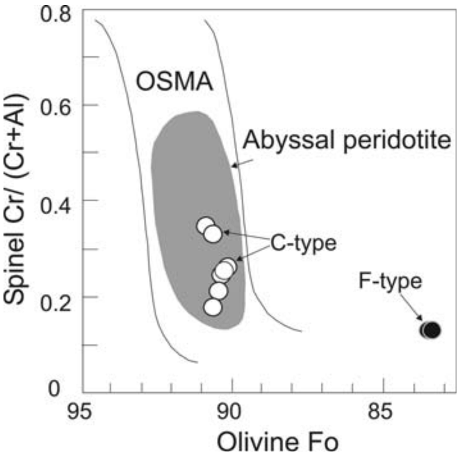

Fig. 7 Relationships between the Fo contents of olivine and Cr# values of spinel in peridotite xenoliths from C-type (*open circles*) and F-type peridotites (*solid circles*) in Cerro del Fraile. Note the F-type peridotites plot outside the olivine-spinel mantle array (OSMA; Arai 1994), suggesting they are not primary mantle peridotites. It also shows the field of abyssal peridotite as a shaded area (Arai 1994)

amphiboles or veins, but clinopyroxene grains have elevated contents of fluid-mobile elements and low Nb and Zr (Fig. 8a). The data suggest that they have undergone cryptic metasomatism by slab-derived aqueous fluids. Considering the tectonic history of the area, this metasomatism most likely took place in early-middle Miocene when the Nazca plate was being subducted beneath the area.

F-type peridotites

F-type xenoliths are very distinct from the C-type xenoliths. Olivine and pyroxenes are low in Mg. Spinel contains low Cr (Figs. 4, 5), and they plot outside the olivine-spinel mantle array of Arai (1994) (Fig. 7), suggesting that they are not typical mantle peridotites. Low Mg in minerals suggest that F-type may be cumulates or the product of metasomatism by an agent with low Mg# and Cr. The first possibility is discounted because cumulates should have only one or two early crystallizing minerals that fractionated from parental magmas, such as websterite veins in C-type xenoliths. F-type peridotites contain olivine, two pyroxenes and large (up to 2 mm) patches of solidified "melt" (~10 vol%) that was once low Mg pargasitic amphibole (Fig. 2e). A rock with all these coarse crystalline minerals is not a cumulate because it requires a substantial evolution of parental melt. Second, spinel in F-type peridotites shows a restricted range in Cr# (~0.13) in different samples. Spinel in cumulates commonly shows a wide range in Cr# because Cr contents in melt rapidly change during the crystallization of spinel (Dick and Bullen 1984; Barnes and Roeder 2001). Third, spinel compositions show low Cr# and Mg#, far from the field of arc-cumulates in the diagram of Al_2O_3–Cr_2O_3 (Fig. 9).

Therefore, we suggest that the F-type peridotites are a product of extensive metasomatism of mantle peridotites. Their low Cr# in spinel and low Mg# in silicate minerals reflect the character of the metasomatizing agent. Considering the compositional change in Cr and Al in spinel, we suggest that the metasomatizing agent was most likely melt instead of fluid alone. The nature of the metasomatizing melt is evaluated based on Mg# of olivine using the Fe–Mg exchange coefficient, K_d, between olivine and melt. The value of K_d is a function of temperature, pressure, and compositions of the olivine and melt (Toplis 2005). The effect of pressures on K_d is small (~0.01 per GPa). However, the concentrations of silica and alkalis of melts and the temperature of the melt may affect K_d under high pressures. Since high degrees of partial melting occur

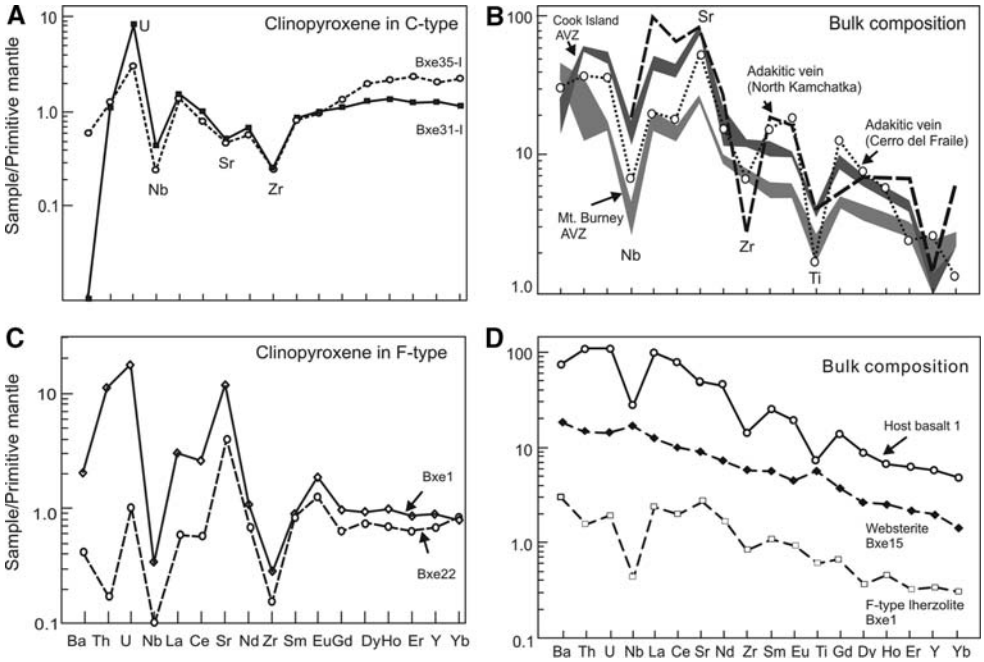

Fig. 8 Primitive mantle-normalized element patterns of minerals, solidified melt, adakitic magmas and bulk rock compositions of host basalts and websterites; **a** representative clinopyroxene (Cpx) in samples Bxe35-I and Bxe31-I of C-type xenoliths, **b** representative clinopyroxene in samples Bxe22 and Bxe1 of F-type xenoliths, **c** adakitic melt in sub-arc mantle xenoliths from Cerro del Fraile xenoliths (Kilian and Stern 2002; Table 4) and north Kamchatka arc (Kepezhinskas et al. 1995), and adakitic volcanic rocks in Mt. Burney and Cook Island, AVZ (Stern and Kilian 1996), **d** bulk compositions of representative host basalts (host-1) (this study; Table 4), websterite (Bxe15) (this study; Table 4) and F-type lherzolite (Bxe1) (Kilian and Stern 2002). Primitive mantle values are from McDonough and Sun (1995)

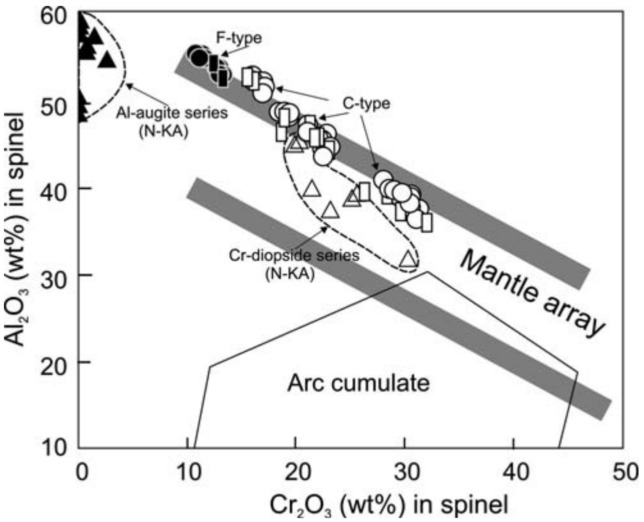

Fig. 9 Al_2O_3 versus Cr_2O_3 in spinel for mantle xenoliths from Cerro del Fraile. Symbols are the same as Fig. 4. Also shown are fields of sub-arc mantle xenoliths of Cr-diopside series and Al-augite series from north of Kamchatka arc (N-KA) (Kepezhinskas et al. 1995)

at high temperature (increasing K_d), but such melt is generally poor in silica (lowering K_d), these effects cancel each other out resulting in a K_d value close to 0.30, which is commonly observed in natural systems (Roeder and Emslie 1970). Considering the above factors, we used a K_d value of 0.30 for the calculation. The hypothetical melt that metasomatized the F-type xenoliths thesefore has Mg# of ~0.60. This value is lower than the Mg# of normal mid-oceanic ridge basalts, ~0.64 (Hofmann 1988). The low Mg# values of the hypothetical melt suggest that the metasomatizing melt for F-type xenoliths is most likely a slab melt.

Slab-derived melt is Si-rich compared to mantle-derived melt. Therefore, the interaction of mantle peridotites with slab-melt commonly results in the formation of secondary orthopyroxene at the expense of olivine as described in metasomatized peridotites from Kamchatka (Arai et al. 2003) and Batan Island, Philippines (Schiano et al. 1995; Arai et al. 2004). The experimental results by Rapp et al. (1999) also suggest the formation of low Mg orthopyroxene after olivine in peridotites during the interactions with slab melt at high melt/rock ratios. We consider that orthopyroxene grains in our F-type peridotites most likely formed from olivine during the reactions with slab-melt because they show low Mg values and extensive re-crystallization texture. Furthermore, this is consistent with the relatively low abundance of olivine in F-type peridotites compared to C-type peridotites. The amount of orthopyroxene is expected to be high when peridotites undergo extensive metasomatism, but the amount of orthopyroxene likely varies depending on the effective ratios of melt to peridotites. Rapp et al. (1999) suggest that peridotites show varying effects from hybridization of the melt to cryptic metasomatism depending on the effective melt/rock ratios. Considering the extensive modification of mineral compositions and the formation of amphiboles, we suggest that the F-type peridotites were metasomatized by slab melt at a moderately high melt/rock ratio.

The metasomatism of sub-arc mantle peridotites by slab-melt is documented in xenoliths in Batan Island, Philippines (Schiano et al. 1995). It produced polygonal low Mg olivine and orthopyroxene neoblasts with the development of mosaic textures, and pargasitic amphibole (Schiano et al. 1995). Another well-documented example is in the north Kamchatka arc (Kepezhinskas et al. 1995, 1996). The mantle xenoliths from the north Kamchatka arc are classified into Cr-diopside series and Al-augite series based on pyroxene compositions (Kepezhinskas et al. 1995). Cr-diopside series xenoliths represent peridotites that were metasomatized by fluids released from slabs. Their spinel is characterized by high Cr#, low Mg and slightly elevated Fe^{3+} common in sub-arc mantle peridotites (Figs. 5, 9). Al-augite series xenoliths are interpreted as being formed during the interaction with Si-rich melt (Kepezhinskas et al. 1995). They contain green spinel with low Cr_2O_3 (<2 wt%) (Figs. 5, 9), suggesting that the spinel was enriched with Al and depleted of Cr during metasomatism with a slab-melt. In terms of the compositions of the spinel and the metasomatic agent, F-type peridotites in Cerro del Fraile are similar to the Al-augite series xenoliths from the north Kamchatka arc (Figs. 5, 9). Furthermore, veins with high SiO_2 (67 wt%) and Al, low Ti and high Na/K ratios of 3–5 in Al-augite series xenoliths were interpreted as solidified slab ‘‘melt’’ (Kepezhinskas et al. 1995), which is comparable to the adakitic veins from Cerro del Fraile as described by Kilian and Stern (2002) (Table 4).

Our proposed interpretation is further supported by high Sr/Y in clinopyroxene and bulk composition of F-type peridotites (Fig. 8b–d). High Sr/Y ratios are one of the characteristic features of slab-melt (Defant and Drummond 1990).

Metasomatism of the mantle below Cerro del Fraile by slab-melt likely took place after the late Miocene as the Nazca plate became younger during the time when the Chile ridge was approaching the trench.

Oxidation state of C-type peridotites

The sub-arc mantle overlying the subducted oceanic crust is generally considered to be oxidized, with

ΔFMQ +0.3 to +2.0. Examples include Ichinomegata in Japan, Marelava in Vanuatu arc, Grenada in Lesser Antilles arc, Santa Isabel and San Jorge in Solomon islands and the Simcoe area in Cascade arc (Wood and Virgo 1989; Ballhaus et al. 1991; Brandon and Draper 1996; Parkinson and Arculus 1999; Parkinson et al. 2003) (Fig. 6). The oxidized condition of mantle wedges is explained by the introduction of oxidizing aqueous fluids liberated from downgoing oceanic slabs (Arculus 1985; Wood and Virgo 1989; Brandon and Draper 1996; Parkinson and Arculus 1999). This is consistent with slightly elevated fO_2 values, ΔFMQ +0.1 to +0.3, of most anhydrous C-type peridotites without ''melt'' patches because these peridotites are interpreted to have undergone cryptic metasomatism by aqueous fluids released from slabs, based on the enrichment of fluid-mobile elements (Fig. 8a). The narrow spread in fO_2 of the samples and the lack of correlation between Cr# of spinel and fO_2 (Fig. 6) may suggest that this cryptic metasomatism homogenized fO_2 values of the peridotites.

The two ''melt''-bearing C-type samples that were metasomatized by an asthenospheric mantle-derived melt, show fO_2 slightly below FMQ. The results are consistent with the fO_2 of the asthenospheric mantle near the FMQ buffer (Taylor and Green 1987; Ballhaus 1993).

Oxidation state of F-type peridotites metasomatized by slab melt

The F-type peridotites record low fO_2 values. The F-type xenolith has undergone extensive recrystallization and intensive metasomatism by slab-melt. All silicate minerals contain low Mg# than usual mantle peridotites. Therefore, it is reasonable to consider that low fO_2 values were acquired during the metasomatism and that the metasomatism by slab-melt was accompanied by lowering of fO_2. This proposed interpretation requires a reducing nature of this slab-melt. This appears to be in conflict with a generally oxidized nature of oceanic crust, which is weathered on the oxidizing sea floor and altered by interactions with oxidizing sea water. The subducted slab is overlain by wet sediments, which likely fuse during the slab melting of underlying oceanic crust. Sediments contain water, carbonate and organic matter and the fusion produces melt and aqueous fluids high in CO_2 and CH_4. The abundance of these volatiles in aquous fluids is controlled by the following reactions:

$$C + O_2 = CO_2 \tag{1}$$

$$C + 2H_2O = CH_4 + O_2 \tag{2}$$

Reaction (1) shows that the presence of organic matter imposes an upper limit of fO_2 of fluids. The upper stability field of graphite is estimated to be close to the FMQ buffer in natural systems because other volatile species may lower the activities of CO_2 and CO and allow the stable occurrence of graphite (Wood et al. 1990; Fig. 10). Reaction 2 shows the formation of CH_4 in aqueous fluids from graphite. The equation suggests that the heating and fusion of organic-rich wet sediments produce CH_4. The relationship between fO_2 and a fraction of CH_4 in the aqueous fluids coexisting with graphite is shown in Fig. 10. Fluids high in CO_2 occur at high fO_2, whereas fluids high in CH_4 occur at low fO_2. The figure also shows that the hypothetical fluids in equilibrium with the F-type xenoliths must have contained CH_4.

The pelagic sediments in the Chile trench contain little or no carbonates, but abundant bitumens and kerogen and evidence of hydrocarbon formation at depths (Behrmann et al. 1992). This is in contrast to the high carbonate content of common oceanic pelagic sediments (Plank and Langmuir 1998). The evidence suggests that aqueous fluids released from sediments in the area likely contained CH_4, and the melt formed

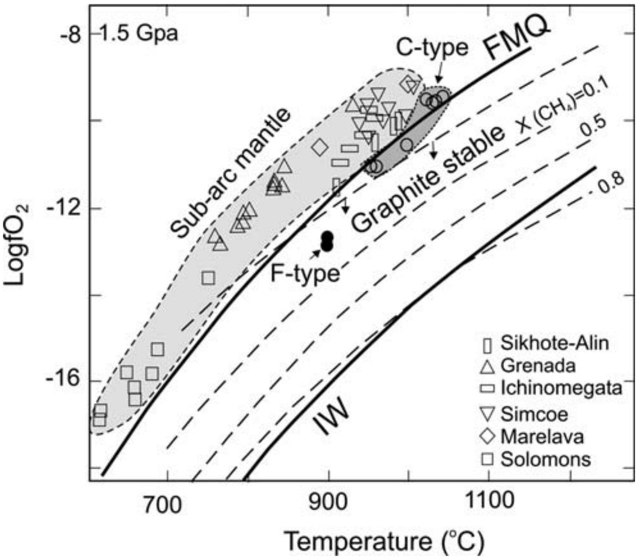

Fig. 10 Fraction of CH_4 in C-H-O fluids on a diagram of fO_2 vs. temperatures (modified after Wood et al. 1990). The values for mantle xenoliths from Cerro del Fraile (this study) are compared to those from other sub-arc mantles; Sikhote-Alin, Russia (Ionov and Wood 1992), Simcoe (Brandon and Draper 1996), Ichinomegata, Japan (Wood and Virgo 1989), Grenada, Marelava, and Solomon islands (Parkinson and Arculus 1999; Parkinson et al. 2003). IW= iron-wustite buffer. Note that the F-type peridotites plot in the field of CH_4-bearing field

from the slab overlain by such sediments was most likely lower in fO_2 because of the CH_4 from organic matter, which maintains a low fO_2 in the fused sediment and slab melt. Reducing fluids together with the slab-melt ascended into the overlying mantle and contributed to lowering fO_2 of the F-type Cerro del Fraile peridotites.

Sediments are generally high in U, especially organic-rich sediments because U^{6+} dissolved in sea water can be fixed as U^{4+} in the organic-rich, reduced sediments (Klinkhammer and Palmer 1991). Therefore, the fusion of sediments and subsequent mixing with a slab-melt produces a melt with elevated concentrations of U. The metasomatism of mantle peridotites by such a melt would produce high U. We consider the high content of U in clinopyroxene in F-type peridotites as another line of evidence for the contribution of sediments to the slab melt that metasomatized these xenoliths (Fig. 8c). For example, clinopyroxene in sample BXe1 shows more than two times higher U content than that of U-rich C-type samples (Fig. 8c).

Average pelagic sediments on the ocean floor consist of 72 vol% carbonate ooze, 19 vol% red clay, and 9 vol% siliceous ooze, and contain approximately 12 wt% CO_2 and 5 wt% H_2O bound in mineral structures plus up to 50 vol% H_2O in pore spaces (Peacock 1990). Oceanic basalts that are altered on and near sea floor also contain abundant carbonates and hydrous minerals. Therefore, subducted slabs in many locations release CO_2–H_2O fluids. This is consistent with the overall oxidized nature, above FMQ, of mantle wedges. But subducted sediments vary depending on locations (Plank and Langmuir 1998). This suggests that the sub-arc mantle would have different fO_2 depending on the type of subducted sediments. This is further supported by a recent finding of unusually oxidized nature of the mantle wedge in the Himalayas where evaporitic sulfates are subducted (Hattori et al. 2005).

Our data suggest that subducted sediments may be important in controlling the redox condition of mantle wedges. In most subduction zones, fluids are released from slabs and sediments to overlying mantle wedges. CO_2 and H_2O are predominant species in the fluids and they maintain relatively high fO_2 of overlying mantle wedges. In subduction zones involving young slabs, partial melting of the slabs and fusion of overlying sediments take place. When the sediments contain high contents of organic matter, the fluids and melt reduce with high CH_4. The ascent of the slab melt and accompanying fluids could significantly lower fO_2 of the overlying mantle peridotites.

Acknowledgements This work was supported by a NSERC Discovery grant to K. H. Hattori and an Ontario Graduate Scholarship in Science and Technology and the University of Ottawa Excellence Scholarship to J. Wang. We thank J-P. Li for allowing us to use the spinel standards prepared by B. J. Wood and D. Virgo. Thanks are also given to L. Shi for his help during the electron microprobe analysis at McGill University. The manuscript benefited from the constructive comments by J. Hoefs, S. Arai and an anonymous journal reviewer.

References

Abe N, Arai S, Yurimoto H (1998) Geochemical characteristics of the uppermost mantle beneath the Japan island arcs: implications for upper mantle evolution. Phys Earth Planet Int 107:233–248

Arai S (1994) Characterization of spinel peridotites by olivine-spinel compositional relationships: review and interpretation. Chem Geol 111:191–204

Arai S, Ishimaru S, Okrugin VM (2003) Metasomatized harzburgite xenoliths from Avacha volcano as fragments of mantle wedge of the Kamchatka arc: implication for the metasomatic agent.Island Arc 12:233–246

Arai S, Takada S, Michibayashi K, Kida M (2004) Petrology of peridotite xenoliths from Iraya volcano, Philippines, and its implication for dynamic mantle-wedge processes. J Petrol 45:369–389

Arculus RJ (1985) Oxidation status of the mantle: past and present. Annu Rev Earth Planet Sci 13:75–95

Ballhaus C (1993) Redox states of lithospheric and asthenospheric upper mantle. Contrib Mineral Petrol 114:331–348

Ballhaus C, Berry RF, Green DH (1991) High pressure experiment calibration of the olivine–orthopyroxene–spinel oxygen barometer: implications for the oxidation state of the mantle. Contrib Mineral Petrol 107:27–40

Ban M, Witt-Eickschen G, Klein M, Seck HA (2005) The origin of glasses in hydrous mantle xenoliths from the West Eifel, Germany: incongruent break down of amphibole. Contrib Mineral Petrol 148:511–523

Barnes SJ, Roeder PL (2001) The range of spinel compositions in terrestrial mafic and ultramafic rocks. J Petrol 42:2279–2302

Barsdell M, Smith IEM (1989) Petrology of recrystallized ultramafic xenoliths from Merelava volcano, Vanuatu. Contrib Mineral Petrol 102:230–241

Behrmann JH, Lewis SD, et al. (1992) Proceedings of the ocean drilling program, Initial Reports, College Station, Texas (Ocean drilling program),141, 807 pp

Brandon AD, Draper DS (1996) Constraints on the origin of the oxidation state of the mantle overlying subduction zones: an example from Simcoe, Washington, USA. Geochim Cosmochim Acta 60:1739–1749

Brey GP, Köhler T (1990) Geothermobarometry in four-phase lherzolites II. New thermobarometers, and practical assessment of existing thermobarometers. J Petrol 31:1353–1378

Bryndzia LT, Wood BJ (1990) Oxygen thermobarometry of abyssal spinel peridotites: the redox state and the C–H–O volatile composition of the Earth's sub-oceanic mantle. Am J Sci 290:1093–1116

Cande SC, Leslie RB (1986) Late cenozoic tectonics of the southern Chile trench. J Geophys Res 91:471–496

Carlson RW, Pearson DG, James DE (2005) Physical, chemical, and chronological characteristics of continental mantle. Rev Geophys 43:1–24

Conceição RV, Green DH (2004) Derivation of potassic (shoshonitic) magmas by decompression melting of phlogopite + pargasite lherzolite. Lithos 72:209–229

Defant MJ, Drummond MS (1990) Derivation of some modern arc magmas by melting of young subducted lithosphere. Nature 347:662–665

DeHoog JCM, Hattori KH, Hoblitt RP (2004) Oxidized sulfur-rich mafic magma at Mount Pinatubo, Philippines. Contrib Mineral Petrol 146:750–761

Dick HJB, Bullen T (1984) Chromian spinel as a petrogenetic indicator in abyssal and alpine-type peridotites and spatially associated lavas. Contrib Mineral Petrol 86:54–76

D'Orazio M, Agostini S, Mazzarini F, Innocenti F, Manetti P, Haller MJ, Lahsen A (2000) The Pali Aike Volcanic Field, Patagonia: slab-window magmatism near the tip of South America. Tectonophysics 321:407–427

Francis DM (1976) The origin of amphibole in lherzolite xenoliths from Nunivak Island, Alaska. J Petrol 17:357–378

Gorring ML, Kays SM, Zeitler PK, Ramos VA, Rubiolo D, Fernandez MI, Panza JL (1997) Neogene Patagonian plateau lavas: continental magmas associated with ridge collision at the Chile triple junction. Tectonics 16:1–17

Hattori KH, and Guillot S (2003) Volcanic fronts as a consequence of serpentinite dehydration in the mantle wedge. Geology 31:525–528

Hattori K, Takahashi Y, Guillot S, Johanson B (2005) Occurrence of arsenic (V) in forearc mantle serpentinites based on X-ray absorption spectroscopy study. Geochim Cosmochim Acta 69:5585–5596

Hofmann AW (1988) Chemical differentiation of the Earth: the relationship between mantle, continental crustal, and oceanic crust. Earth Planet Sci Lett 90:297–314

Ionov DA, Wood BJ (1992) The oxidation state of subcontinental mantle: oxygen thermobarometry of mantle xenoliths from Central Asia. Contrib Mineral Petrol 11:179–193

Kay SM, Ramos VA, Marquez M (1993) Evidence in Cerro Pampa volcanic rocks for slab-melting prior to ridge-trench collision in southern South America. J Geol 101:703–714

Kepezhinskas PK, Defant MJ, Drummond MS (1995) Na metasomatism in the island-arc mantle by slab melt-peridotite interaction: evidence from mantle xenoliths in the north Kamchatka arc. J Petrol 36:1505–1527

Kepezhinskas PK, Defant MJ, Drummond MS (1996) Progressive enrichment of island arc mantle by melt-peridotite interaction inferred from Kamchatka xenoliths. Geochim Cosmochim Acta 60:1217–1229

Kilian R, Stern CR (2002) Constraints on the interaction between slab melts and the mantle wedge from adakitic glass in peridotite xenoliths. Eur J Mineral 14:25–36

Klinkhammer GP, Palmer MR (1991) Uranium in the oceans: where it goes and why. Geochim Cosmochim Acta 55:1799–1806

Lee C-TA (2005) Trace element evidence for hydrous metasomatism at the base of the North American lithosphere and possible association with Laramide low-angle subduction. J Geol 113:673–685

McDonough WF, Sun SS (1995) The composition of the Earth. Chem Geol 120:223–253

Mibe K, Fujii T, Yasuda A (1999) Control of the location of the volcanic front in island arcs by aqueous fluid connectivity in the mantle wedge. Nature 401:259–262

Nell J, Wood BJ (1991) High-temperature electrical measurements and thermodynamic properties of Fe_3O_4–$FeCr_2O_4$–$MgCr_2O_4$–$FeAl_2O_4$ spinels. Am Mineral 76:406–426

Parkinson IJ, Arculus RJ (1999) The redox state of subduction zones: insights from arc-peridotites. Chem Geol 160:409–423

Parkinson IJ, Arculus RJ, Eggins SM (2003) Peridotite xenoliths from Grenada, lesser Antilles Island arc. Contrib Mineral Petrol 146:241–262

Peacock SM (1990) Fluid processes in subduction zones. Science 248:329–336

Plank T, Langmuir CH (1998) The chemical composition of subducting sediment: implications for the crust and mantle. Chem Geol 145:325–394

Qi Q, Taylor LA, Zhou XM (1995) Petrology and geochemistry of mantle peridotite xenoliths from SE China. J Petrol 36:55–79

Rapp RP, Shimizu N, Norman MD, Applegate GS (1999) Reaction between slab-derived melts and peridotite in the mantle wedge: experimental constraints at 3.8 GPa. Chem Geol 160:335–356

Roeder PL, Emslie RF (1970) Olivine-liquid equilibrium. Contrib Mineral Petrol 29:275–289

Schiano P, Clocchiatti R, Schimizu N, Maury RC, Jochum KP, Hofmann AW (1995) Hydrous, silica-rich melts in the sub-arc mantle and their relationship with erupted arc lavas. Nature 377:595–600

Shaw CSJ, Klügel A (2002) The pressure and temperature conditions and timing of glass formation in mantle-derived xenoliths from Baarley, Western Eifel, Germany: the case for amphibole breakdown, lava infiltration and mineral-melt reaction. Mineral Petrol 74:163–187

Sinigoi S, Comin-Chiaramonti P, Alberti AA (1980) Phase relations in the partial melting of the Baldissero spinel-lherzolite (Ivrea-Verbano Zone, Western Alps, Italy). Contrib Mineral Petrol 75:111–121

Stern CR, Kilian R (1996) Role of the subducted slab, mantle wedge and continental crust in the generation of adakites from the Andean Austral Volcanic zone. Contrib Mineral Petrol 123:263–281

Stern CR, Kilian R, Olker B, Hauri EH, Kyser TK (1999) Evidence from the mantle xenoliths for relatively thin (<100 km) continental lithosphere below the Phanerozoic crust of southernmost South America. Lithos 48:217–235

Taylor WR, Green DH (1987) Measurement of reduced peridotite-C-O-H solidus and implications for redox melting of the mantle. Nature 332:349–352

Taylor RP, Jackson SE, Longerich HP, Webster JD (1997) In situ trace-element analysis of individual silicate melt inclusions by laser ablation microprobe-inductively coupled plasma-mass spectrometry (LAM-ICP-MS). Geochim Cosmochim Acta 61:2559–2567

Toplis MJ (2005) The thermodynamics of iron and magnesium partitioning between olivine and liquid: criteria for assessing and predicting equilibrium in natural and experimental systems. Contrib Mineral Petrol 149:22–39

Wells PRA (1977) Pyroxene thermometry in simple and complex systems. Contrib Mineral Petrol 62:129–139

Wood BJ, Virgo D (1989) Upper mantle oxidation state: ferric iron contents of lherzolite spinels by 57Fe Mössbauer spectroscopy and resultant oxygen fugacities. Geochim Cosmochim Acta 53:1277–1291

Wood BJ, Bryndiza LT, Johnson KE (1990) Mantle oxidation state and its relationship to tectonic environment and fluid speciation. Science 248:337–345

Woodland AB, Kornprobst J, Wood BJ (1992) Oxygen thermobarometry of orogenic lherzolite massifs. J Petrol 33:203–230

Yaxley GM, Kamenetsky V (1999) In situ origin for glass in mantle xenoliths from southeastern Australia: insights from trace element compositions of glasses and metasomatic phases. Earth Planet Sci Lett 172:97–109

Yaxley GM, Kamenetsky V, Green DH, Falloon TJ (1997) Glasses in mantle xenoliths from western Victoria, Australia, and their relevance to mantle processes. Earth Planet Sci Lett 148:433–446